A Geometric Polarization Rotation Model for the 3-D Spatial Channel Model

Stephan Jaeckel, *Member, IEEE*, Kai Börner, *Student Member, IEEE*, Lars Thiele, *Member, IEEE*, and Volker Jungnickel, *Member, IEEE*

***Abstract*—It is common to use channel models such as the 3GPP spatial channel model (SCM), the WINNER model or ray tracing to evaluate multiple-antenna multiple-user techniques in wireless communications. Cross-polarized antennas can enhance the channel rank and thus the throughput of such systems especially in case of a line-of-sight (LOS) connection. This requires an exact model of the polarization characteristics. To increase the accuracy of the existing channel models, we propose a new method that predicts the polarization state of a microwave link based on findings in the field of optics. We verified the method by cross-polarized multiple-input–multiple-output (MIMO) measurements at 2.6 GHz with 16 transmitters and ten receivers in an urban macrocell environment under strong LOS conditions in downtown Berlin, Germany. Comparisons of simulation and measurement results show that the coefficients of the polarized LOS channel can be predicted very well by the new method. Measured capacities at 10-dB signal-to-noise ratio (SNR) were in between 14.2 and 19.1 b/s/Hz—values that can be predicted by the channel model with more than 90% accuracy. This increase in modeling accuracy is an important feature for many applications such as heterogeneous networks, space-to-ground satellite communications, and cooperative communications.**

***Index Terms*—Capacity, cross-polarization ratio (XPR), dual polarization, measurement, MIMO systems, modeling, multiple-input–multiple-output (MIMO), polarization, radio propagation, spatial channel model (SCM).**

I. Introduction

THE use of multiple-input–multiple-output (MIMO) techniques [1], [2] has attracted considerable attention in the standardization of mobile wireless systems for wide-area coverage [3], [4] where they increase the spectral efficiency and, therefore, the revenue that operators can realize with a limited bandwidth. When applying MIMO in cellular networks there is a great interest in validating the achievable gains and comparing the performance among multiple vendors before any new proposal is standardized. Realistic channel modeling is thus a prerequisite for a fair comparison. It is common to use the 3GPP spatial channel model (SCM) [5] for this task. The SCM is geometry based and, thus, it models the scattering environment by a set of discrete reflections—similar to ray tracing. During the European Wireless World Initiative New Radio (WINNER) projects, the model was extended for many different scenarios [6]–[9]. The WINNER model is also used as a guideline for the evaluation of radio interface technologies in the International Telecommunication Union (ITU) [10], [11].

If one uses MIMO in urban cellular setups, measurements show that the single-link MIMO capacity tends to degrade when there is a free line of sight (LOS) between the transmitter and the receiver [12], [13]. In this case, it is helpful to exploit multiple polarizations to increase the number of spatial degrees of freedom especially when using compact antennas with a limited amount of elements [14], [15]. However, if we use the WINNER model with a strong LOS component, the measured characteristics cannot be fully reproduced. It has been shown that feedback reports from mobile terminals with cross-polarized antennas may be incorrect if they are obtained from the WINNER model [16]. This could be explained by some polarization effects that are not fully considered. In the non-line-of-sight (NLOS) case, the polarization effects in the channel are modeled by a 2×2 matrix of complex gains which are scaled by the cross-polarization ratio (XPR). However, Zhou *et al.* [17] already indicated that it might be preferable to model the channel XPR by a rotation matrix. We further discuss later in our paper that the WINNER approach has great similarities with the Jones calculus, a method for handling polarized electromagnetic waves in the field of optics [18]. One necessary condition for applying the calculus, however, is that all elements (e.g., transmit and receive antennas) have to be aligned on one axis. This condition is rarely fulfilled in the considered scenarios which might lead to partially incorrect results also for the LOS link.

This has several implications. First, when cellular networks are deployed more densely, the probability of a free LOS tends to increase [19]. Thus, polarization effects become more important. Second, current developments in cellular networks use in-band relays to increase the capacity. These relays are connected to a base station (BS) via a backhaul link, which is often realized by a fixed LOS connection. The capacity of this link depends on the correct modeling of the polarization characteristics. Third, current multibeam satellite networks increasingly require the use of cellular evaluation tools in order to model the interference between the beams when targeting unitary frequency reuse. In this case, the huge distance between the transmitter and the receiver implies that the angular spread at the transmitter is almost zero. Reception also often depends on a free LOS. Thus, MIMO gains can only be realized through polarization multiplexing.

Manuscript received February 29, 2012; revised June 20, 2012; accepted August 08, 2012. Date of publication August 17, 2012; date of current version November 29, 2012. This work was supported by the German Federal Ministry of Economics and Technology (BMWi) in the national collaborative project IntelliSpektrum under Contract 01ME11024, by the European Space Research and Technology Centre (ESTEC) under Contract AO/1-5985/09/08/NL/LvH (Acronym: MIMOSA), and by the German Federal Ministry of Education and Research (BMBF) under Contract 01BU0631 (Acronym: EASY-C).

The authors are with the Fraunhofer Institute for Telecommunications, Heinrich Hertz Institute (HHI), Berlin D-10587, Germany (e-mail: stephan.jaeckel@hhi.fraunhofer.de).

Digital Object Identifier 10.1109/TAP.2012.2214017

First attempts to include polarization effects into the SCM were made by Shafi *et al.* [21] who extended the simple 2-D antenna pattern of the SCM to a dual-polarized 3-D pattern. This method was then also adopted for the WINNER model [25]. However, Shafi *et al.*'s approach did not include a geometry-based method to calculate the cross-polarization effects. Instead, the XPR was incorporated statistically where the parameters were derived from measurements. This statistical approach is shown to lead to correct results for the cross-polarization discrimination (XPD)[1] in case of a well-balanced statistical mixture between LOS and NLOS scenarios in an indoor environment. However, the distribution of singular values which is better suited for characterizing the multistream capabilities of MIMO channels has not been considered.

Later, Quitin *et al.* [26] introduced an analytical channel model that correctly takes the antenna orientation into account. However, this method is limited to azimuthal propagation only (i.e., no elevation angles are supported), and it does not support arbitrary antenna characteristics. We also proposed a geometric polarization model [13] that could correctly predict the capacity of a specific measurement setup. It supports elevation angles, but no flexible antennas. Moreover, the correct calculation of the polarized MIMO channel required a large number of coordinate transformations, which complicates the implementation. A simplified version of this model [27] is compatible with the SCM but lacks precision and also has restrictions on the antenna configuration.

This paper provides a new approach that correctly incorporates the cross-polarization characteristics of the LOS link. Our method is based on the Jones calculus [18], and we propose a method to calculate the channel XPR by using an algorithm inspired thereby. The new method was validated by outdoor measurements in downtown Berlin, Germany. The measured and simulated 10×16 cross-polarized MIMO channels have two dominant degrees of freedom due to the polarization. The received power on differently oriented antenna elements fits very well the measurement results and capacities that can be predicted within 90% accuracy. The remainder of this paper is organized as follows. Section II introduces the new polarization model. Then, Sections III and IV describe the experimental setup and the results, respectively.

II. Geometric Model for Polarized Channels

A. A Short Introduction to the SCM

The SCM [5] can be understood as a "statistical ray-tracing method." Unlike in classical ray tracing, it does not use an exact geometric representation of the environment but distributes the positions of the scatterers (the sources of indirect signals such as buildings or trees) randomly. A simplified overview of the model is depicted in Fig. 1. For each path, the model derives the angle of departure (the angle between the transmitter and the scatterer), the angle of arrival (the angle between the receiver and the scatterer), and the total path length d, which results in a delay τ of the signal. For the sake of simplicity, only two paths

[1]Following the definition in [24], we use the term XPR for the polarization effects in the channel. Combining the XPR with imperfect antennas yields a global XPD.

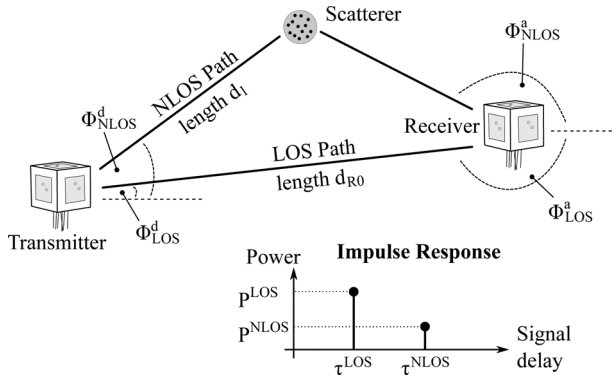

Fig. 1. Simplified overview of the 2-D modeling approach used in the SCM.

are shown in the figure. Normally, the SCM uses six paths, and the WINNER model uses up to 20. The output is an ordered list of complex-valued Dirac functions at a specific delay. If the simulation contains a LOS component, then this path has always the shortest length and thus arrives first at the receiver. When there are no obstructions, then that signal is also dominant in the impulse response.

One major advantage of the SCM is that it allows the separations of propagation and antenna effects. An antenna is defined by its directional response F, also known as field pattern. The original SCM considers only 2-D propagation. Thus, F is a function of the azimuth angle ϕ, which is also indicated in Fig. 1. Later extensions [21] also consider the elevation direction θ. The complex amplitude g of one path between a transmit antenna t and a receive antenna r notes

$$g_{r,t} = \sqrt{P} \cdot \mathbf{F}_r(\phi^a, \theta^a)^T \cdot \mathbf{M} \cdot \mathbf{F}_t(\phi^d, \theta^d) \cdot e^{-j\frac{2\pi}{\lambda} \cdot d} \qquad (1)$$

where $\mathbf{F}_r$ and $\mathbf{F}_t$ describe the polarimetric antenna response at the receiver and the transmitter, respectively. λ is the wavelength, P is the power of the path, (ϕ^a, θ^a) are the arrival angles, and (ϕ^d, θ^d) are the departure angles. $\mathbf{F}(\phi, \theta)$ is a two-element vector which contains the vertically (F_V) and horizontally (F_H) polarized component of the antenna response

$$\mathbf{F}(\phi, \theta) = \begin{pmatrix} F_V(\phi, \theta) \\ F_H(\phi, \theta) \end{pmatrix}. \qquad (2)$$

$\mathbf{M}$ is the 2×2 polarization coupling matrix. This matrix describes how the polarization changes on the way from the transmitter to the receiver. Note that the physical propagation effects such as the angles of departure and arrival, the path powers, the delays, and the polarization coupling stay the same for all antennas in a MIMO configuration. Only the field patterns and the path length differ for each antenna.

Many references (e.g., [20]–[24]) use an approximation of the polarization effects based on the XPR. The XPR quantifies the separation between two polarized channels due to different polarization orientations. $\mathbf{M}$ is then often modeled by using random coefficients $(z_{vv}, z_{vh}, z_{hv}, z_{hh})$ as

$$\mathbf{M} = \begin{pmatrix} z_{vv} & \sqrt{\frac{1}{\mathrm{XPR}_h}} \cdot z_{vh} \\ \sqrt{\frac{1}{\mathrm{XPR}_v}} \cdot z_{hv} & z_{hh} \end{pmatrix}. \qquad (3)$$

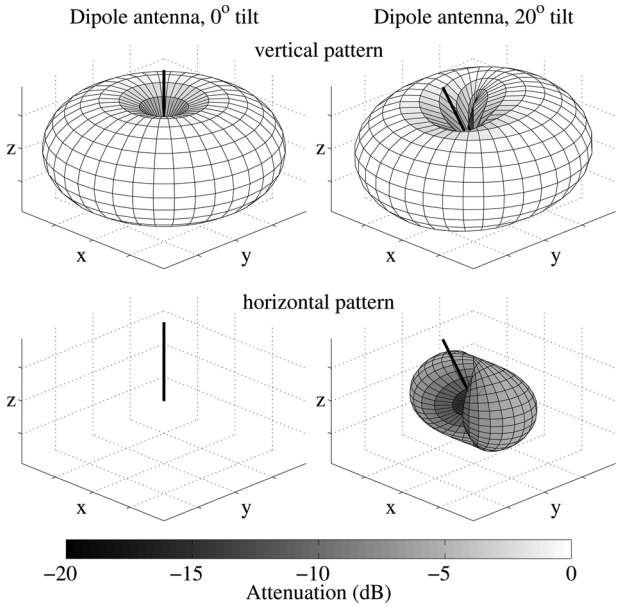

Fig. 2. Example patterns for a dipole antenna.

Our contribution, which is laid out in the following sections, focuses on a new method for calculating $\mathbf{M}$ based on linear transformations.

B. The Antenna Model

The antenna model has an important part in the direct calculation of the channel XPR. Since we want to stay compatible with WINNER, we do not introduce a new antenna model but take advantage of the already existing one [25]. However, all calculations concerning the polarization are done in a global coordinate system (GCS). Hence, our mathematical description differs from [25]. We also introduce an orientation vector $\mathbf{o}$, which is added to the antenna description. This vector indicates the orientation of the antenna after 3-D rotations take place. For example, if we model a dipole, the initial vector points in z-direction, aligned with the vertical polarization. When the antenna is flipped on the side, the vector is turned accordingly.

Orientation changes are desirable in many cases, for example, when tilting BS arrays or changing the orientation of mobile terminals. An example is depicted in Fig. 2. The left-hand side of the figure shows a dipole pattern that has only a vertical component and is in line with the GCS. The right-hand side shows the same antenna tilted by 20° around the x-axis. In order to maintain alignment with the GCS, the antenna pattern is transformed. The resulting pattern also has a horizontal component. The orientation vector for both cases is plotted as a black line. The antenna response (2) can now be obtained by reading the polarimetric beam pattern at the given angles (ϕ, θ). A method to align the polarimetric antenna patterns with the GCS is described in Appendix A. Circular or elliptic polarization can be modeled as a superposition of two linear antennas. This is described in Appendix C.

C. Relation Between the SCM and the Jones Calculus

Jones invented a simple method to calculate polarization effects in optics [18]. In his work, he described the polarization state of a ray of light by the so-called Jones vector. Any object that changes the polarization (or the intensity) of the light is represented by a 2×2 Jones matrix. It was found that the product of the Jones matrix of the optical element and the Jones vector of the incident light accurately describes the polarization state of the resulting ray. Generally, this calculus can be used for any electromagnetic wave. It is especially interesting for the SCM where the paths are handled similarly to optical rays.

In the Jones calculus, the Jones vector contains the x- and y-components of the amplitude and phase of the electric field traveling in the z-direction

$$\begin{pmatrix} E_x(t) \\ E_y(t) \end{pmatrix} = e^{j\omega t} \cdot \underbrace{\begin{pmatrix} A_x e^{j\epsilon_x} \\ A_y e^{j\epsilon_y} \end{pmatrix}}_{\text{Jones vector}}. \tag{4}$$

The same expression is found in the antenna pattern (2) of the WINNER model where the complex value $A_y e^{j\epsilon_y}$ from the Jones vector can be identified with the (generally also complex-valued) vertical component $F_V(\phi, \theta)$ of the antenna pattern. Likewise, $A_x e^{j\epsilon_x}$ can be identified with $F_H(\phi, \theta)$. This implies that the polarization coupling matrix $\mathbf{M}$ in (1) is a Jones matrix and that the Jones calculus could apply also to the WINNER model.

In general, $\mathbf{M}$ can be seen as a transformation operation that maps the incoming signal on the polarization plane to an outgoing signal. If the coefficients are real valued, then linear transformations—such as rotation, scaling, shearing, reflection, and orthogonal projection as well as combinations of those operations—are possible. If the coefficients are complex valued, then the matrix shows characteristics of a Möbius transformation. Such transformations can map straight lines to straight lines or circles and *vice versa*. Since the Jones calculus allows the use of complex coefficients, it can transform linear-polarized signals into circular or elliptical-polarized signals and elliptical-polarized signals to linear-polarized signals. This implies that using (3) with complex coefficients results in a completely random polarization behavior when XPR_v and XPR_h are small (i.e., when the off-diagonal elements are large). When $\text{XPR}_{v,h}$ is large (and the off-diagonal elements are close to zero), then (3) describes a scaling operation.

We propose a different method to model the polarization based on rotation angles. If we consider that the transmitter and the receiver are arranged on the optical axis so that the electric field is perpendicular to this axis, the Jones matrix is given as

$$\tilde{\mathbf{M}}(\vartheta) = \begin{pmatrix} \cos\vartheta & \sin\vartheta \\ -\sin\vartheta & \cos\vartheta \end{pmatrix}. \tag{5}$$

It turns the polarization axis of the wave by an angle ϑ while changing neither the polarization type nor the amplitude. For example, linear-polarized waves remain linearly polarized. In the following, $\tilde{\mathbf{M}}(\vartheta)$ will be calculated explicitly for the LOS component. For the NLOS components, we derive a mapping function that converts the XPR value into a rotation angle.

An example scenario showing the effect of the new method is depicted in Fig. 3. The upper part shows the scenario setup and the lower part shows the results. Both the transmitter and the receiver are equipped with dipole antennas that were initially slanted by 45° around the y-axis. The transmitter is placed 5

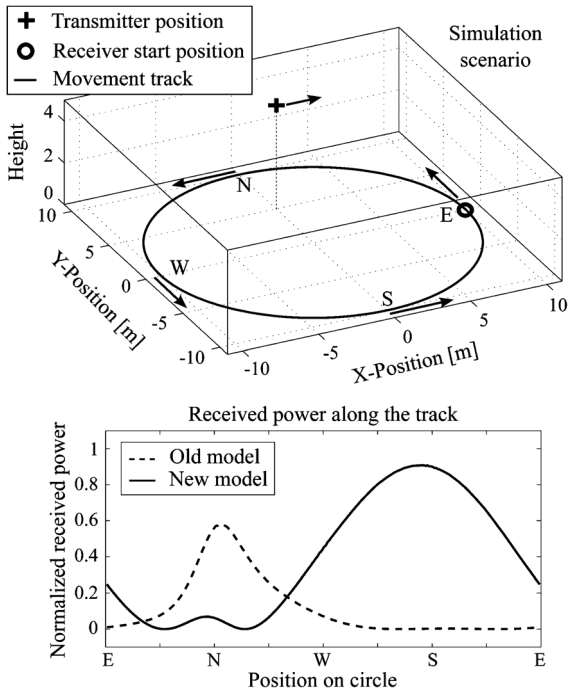

Fig. 3. Example scenario showing the effect of the new method.

m above ground and 5 m north of the scenario center. The receiver then moves counterclockwise around the transmitter with its antenna orientation changing in accordance with the movement direction. The orientations of the transmitter and the receiver (including the movement direction) are indicated by the arrows. The lower figure shows the LOS power along the track. The dashed curve comes from the WINNER approach where the orientation mismatch of the antennas was not taken into account. For example, the polarimetric beam patterns were rotated and interpolated correctly, but no polarization change was assumed along the path. The new model (solid line) calculates the change of the polarization due to the antenna orientation and adjusts the polarization accordingly.

D. Model for the Direct (LOS) Component

One condition for using the Jones calculus is that all polarizing elements need to be arranged on one axis which is perpendicular to the plane of the polarizers. This is hardly applicable in mobile communications due to the placement of the transmitter and the receiver in the environment and the different orientations of the antennas. One possible solution was given in our earlier paper [13] where we used a set of projections to compute the polarization of the direct component. The same principal method can be applied here. However, here we perform all calculations in global Cartesian coordinates which significantly reduces the complexity.

The principle of the model is depicted in Fig. 4. The wave travel direction $\mathbf{r}$ is determined by the angle of arrival (AoA) at the receiver given in azimuth ϕ^a and elevation θ^a direction. The transmit polarization vector $\mathbf{F}_t$ results from the beam pattern (2) and lies in the plane perpendicular to $\mathbf{r}$. The receive antenna can have any orientation in 3-D space. Thus, we need additional information on the element orientation which is realized by the orientation vector $\mathbf{o}_r$. However, this vector does

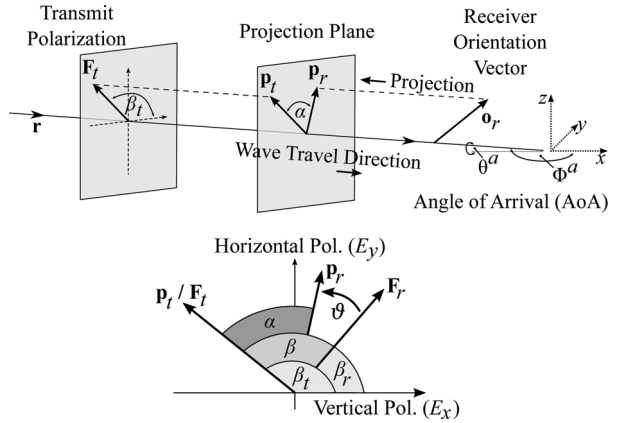

Fig. 4. Illustration of the angles and vectors used for the computation of the geometric LOS polarization; Top: Scheme of the projection. Bottom: Angles on the projection plane.

not lie in the same plane as $\mathbf{F}_t$ does. The polarization vector $\mathbf{p}_r$ results from a projection of $\mathbf{o}_r$ on the plane perpendicular to the travel direction. Due to the orientation mismatch between the transmitter and the receiver, there will be an offset between $\mathbf{p}_r$ and the vector obtained from the receiver beam pattern $\mathbf{F}_r$, which is indicated in the lower part of Fig. 4. We compensate for it by introducing a Jones matrix (5) that turns the polarization of the receive antenna to match the value obtained from the projection. Thus, we have to determine the rotation angle ϑ. This is done by explicitly calculating the angles β_t, β_r, and α from Fig. 4 and computing ϑ as

$$\vartheta = \beta_t - \beta_r - \alpha. \tag{6}$$

The procedure[2] for this calculation is described in Appendix B.

E. Model for the Indirect Components

For the NLOS components, the transmitted signal undergoes some diffraction, reflection, or scattering before reaching the receiver. Following the common Fresnel formula in electrodynamics, the polarization direction can be changed at the boundary surface between two dielectric media. Svantesson [28] provided a method for modeling the polarization of a reflected wave where the polarization coupling is a function of several geometric parameters such as the orientation of the scatterers. However, these parameters are not generally available in the SCM. In addition to that, only metallic reflections keep the polarization unchanged. Reflections at dielectric media can cause changes of the polarization being a function of the complex-valued dielectric constant of the media and of the angle of incidence. Hence, not only the polarization angle, but also the polarization type might change. In order to address this issue, studies of the polarizations effects in individual scattering clusters in several outdoor and indoor scenarios were done [29]–[31]. The published results indicate that, in many cases, scattering preserves the polarization quiet well. However, since only the powers of the elements in the polarization coupling matrix were analyzed, no conclusions can be drawn on how elliptic the polarization of the scattered wave becomes.

[2]Note here that our method only applies to linear-polarized waves. Circular polarization can be obtained by combining two linear elements with a phase offset (see Appendix C for details).

We assume that the polarization coupling matrix $\mathbf{M}$ for the NLOS components can be described by a combination of linear transformations. Hence, we can take advantage of the existing findings of the XPR. If the XPR is identical for both polarization directions (such as in the WINNER parameter tables), then we can follow the approach from [17] and calculate an additional NLOS rotation matrix $\mathbf{M}_\gamma$ as

$$\mathbf{M}_\gamma = \begin{pmatrix} m_{vv} & m_{vh} \\ m_{hv} & m_{hh} \end{pmatrix} = \begin{pmatrix} \cos\gamma & -\sin\gamma \\ \sin\gamma & \cos\gamma \end{pmatrix}. \quad (7)$$

Following the notations in [24], we get

$$\mathrm{XPR} = \frac{|m_{vv}|^2}{|m_{hv}|^2} = \frac{|m_{hh}|^2}{|m_{vh}|^2} = \frac{(\cos\gamma)^2}{(\sin\gamma)^2} = (\cot\gamma)^2 \quad (8)$$

$$\gamma = \mathrm{arccot}(\sqrt{\mathrm{XPR}}). \quad (9)$$

However, when the XPR is different for the vertical and horizontal components [24], [30], then we get three parameters

$$\mathrm{XPR}_v = \frac{|m_{vv}|^2}{|m_{hv}|^2} \quad \mathrm{XPR}_h = \frac{|m_{hh}|^2}{|m_{vh}|^2} \quad \mathrm{CPR} = \frac{|m_{vv}|^2}{|m_{hh\cdot}|^2}$$

In order to fulfill all three, we can combine two rotations, one for the vertical component and one for the horizontal component, with a scaling operation. We convert XPR_v and XPR_h to rotation angles γ_v and γ_h using (9) and calculate $\mathbf{M}_\gamma$ to

$$\mathbf{M}_\gamma = \begin{pmatrix} \cos\gamma_v & -\tan\gamma_h \cdot \cos\gamma_v \cdot \frac{1}{\sqrt{\mathrm{CPR}}} \\ \sin\gamma_v & \cos\gamma_v \cdot \frac{1}{\sqrt{\mathrm{CPR}}} \end{pmatrix}. \quad (10)$$

Elliptic polarization is obtained, when there is a phase difference κ between the horizontal component and the vertical component. This is included by a scaling matrix

$$\mathbf{M}_\kappa = \begin{pmatrix} 1 & 0 \\ 0 & \exp j\kappa \end{pmatrix}. \quad (11)$$

The antenna-dependent parameters β_r, β_t, and α are handled as in the LOS case using (6), which results in a rotation matrix $\tilde{\mathbf{M}}(\vartheta)$. The transformations are then combined to

$$\mathbf{M} = \frac{\sqrt{2}}{\|\mathbf{M}_\gamma\|_F} \cdot \tilde{\mathbf{M}}(\vartheta) \cdot \mathbf{M}_\gamma \cdot \mathbf{M}_\kappa. \quad (12)$$

The normalization with the Frobenius norm $\|\mathbf{M}_\gamma\|_F$ ensures that $\mathbf{M}$ does not change the power of the multipath component.

III. Experimental and Simulation Setup

The model is validated by measurements on the campus of the Technical University of Berlin (TUB), Berlin, Germany. We used a RUSK HyEff channel sounder [32] at 2.53 GHz with 20-MHz bandwidth to record a 10×16 MIMO channel matrix for different positions of the transmitter and the receiver. The system was set up to record ten channel matrices per half-wavelength with a time window of 6.4 μs for each individual link. The effectively radiated power was $+37$ dBm per antenna and the receiver sensitivity was around -95 dBm.

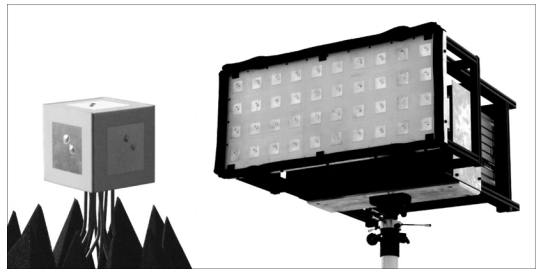

Fig. 5. Measurement antennas. (Left) A compact MIMO cube made from five dual-polarized patch elements was used at the receiver and (right) a ULA assembled from 40 elements at the transmitter.

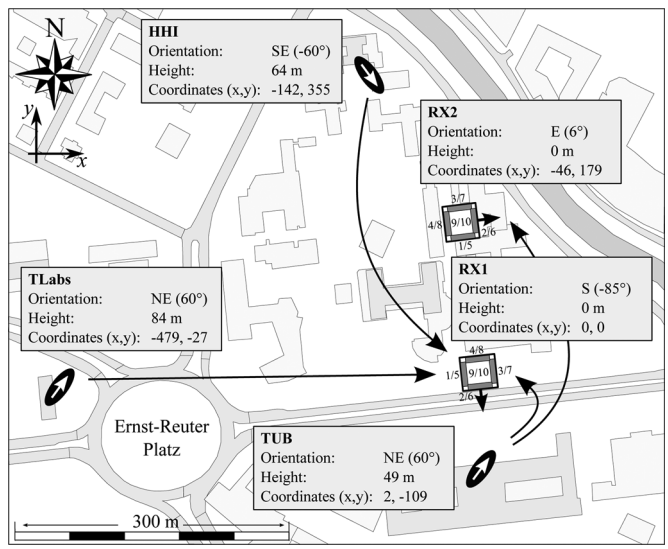

Fig. 6. Campus map with the transmit and receive positions and the orientations of the antennas. The element numbers at the receiver correspond to the row number in the channel matrix (see Fig. 8). The first value is for the vertical polarization, and the second value is for the horizontal polarization.

The antenna arrays at the transmitter and the receiver are made from cross-polarized patches with two points of delivery feeding vertical and horizontal polarization of the same element. The coupling of the two polarizations measured at broadside in an anechoic chamber is less than -30 dB and generally does not exceed -25 dB at the 90° full width at half-maximum (FWHM) beam width. Forty pieces of those patch antennas were assembled into a uniform linear array for the transmitter shown in the right-hand side graph in Fig. 5. Furthermore, four elements in each column are coupled by a power divider to reduce the FWHM in elevation direction to 20°, which leads to an antenna gain of approximately 11 dBi. The left-most and right-most columns in the array are grounded by 50 Ω resistors to minimize edge effects in the array. Therefore, altogether eight columns of cross-polarized patches at $\lambda/2$ spacing result in 16 transmit elements in the MIMO matrix. At the receiver, we assembled the so-called MIMO cube out of five patch elements (see the left-hand side graph in Fig. 5). We used the same terminal antenna configuration already in our earlier measurements [13]. However, here, we scaled the cube to an edge length of 5 cm to fit the patches for 2.53 GHz. A simplified model of the antenna arrays was created for the comparison with simulations. A detailed description of the antenna model is given in Appendix D.

The measurement scenario is depicted in Fig. 6 where the coordinates, heights, and antenna orientations of each transmit and receive position are given. Three positions for the transmitter were chosen around the Ernst Reuter Platz in downtown Berlin, Germany. They are the rooftop of the Heinrich Hertz Institute (HHI), the Deutsche Telekom Laboratories (TLabs), and the main building of the TUB. All in all, we performed four successive LOS measurements. First, we got three channel matrices at position RX1 where there is a direct link to all transmitters. Second, we went to position RX2 and received another link to TUB.

The same scenario was then reconstructed by simulations where the coordinates (in units of meters) given in Fig. 6 served for calculating the wave travel direction. We repeated the simulations 30 times with different initializations of the scatterer positions. For the large-scale parameters, we used default values from the WINNER tables [6], [7] for the urban macrocell scenario. We set the delay spread to 40 ns, the azimuth spread at the transmitter to 10°, and at the receiver to 50°. The corresponding elevation spreads are 5° and 9°. The XPR values for the NLOS components are modeled log-normal distributed with a median value μ_{XPR} of 8 dB and a standard deviation of 4 dB. We used the same value for both vertical (XPR_V) and horizontal (XPR_H) components. The Ricean K-factor (i.e., the power ratio between the LOS path and the sum power of the NLOS paths), however, has a major impact on the performance in a LOS scenario. Thus, we cannot apply standard values from the WINNER tables, but we have to match the values to the measured scenario. This was done by first calculating a singular value decomposition (SVD) [33] of the 10×16 channel matrix $\mathbf{H}_n = \mathbf{U}_n \mathbf{D}_n \mathbf{V}_n^H$. The diagonal matrix $\mathbf{D}_n$ contains at most $n_\lambda = 10$ nonzero singular values λ. Then, we estimated the K-factor from the measurement data to $\tilde{K} = (\lambda_1 + \lambda_2)/(\sum_{i>2} \lambda_i)$. The simulations were run with this initial value, and the singular values were calculated. The same measure $\tilde{K}$ was obtained from the simulation results. If the values did not match, the K-factor setting for the simulation was increased or lowered until both measurement and simulation had the same result for $\tilde{K}$. In this way, we estimated the K-factors in the four scenarios to 3.6 dB for HHI-Rx1, 8.7 dB for TLabs-Rx1, 3.0 dB for TUB-Rx1, and 2.5 dB for TUB-Rx2. For comparison, the value from [6] is 7 dB with a standard deviation of 3 dB. Thus, our values are well within the range specified by WINNER.

From the measurements, we extracted a $10 \times 16 \times 129 \times 200$ complex-valued channel tensor for each of the four scenarios. The four dimensions represent the receive antenna index, the transmit antenna index, the frequency bin, and the snapshot number, respectively. We used a preprocessing technique [14] to get the contributing multipath components for each of the 160 links. Essentially, we calculated L taps from the measured data where

$$\tilde{h}_n = \sum_{l=1}^{L} \underbrace{\alpha_l \cdot e^{j\phi_l}}_{=g_l} \cdot e^{-j2\pi \cdot \frac{n \cdot m_l}{N}} \tag{13}$$

is the channel representation in frequency domain after preprocessing. α_l is the amplitude, ϕ_l is the phase, and m_l is the normalized delay[3] of the lth multipath component. $n = 1, \ldots, N$ is the carrier index and $N = 129$ is the number of carriers. Due to the processing, $\tilde{h}$ has a signal-to-noise ratio (SNR), which is approximately 6 dB better than in the measurement data, since a significant part of the noise can be removed. A similar representation $\hat{h}_n$ of the wireless channel was obtained from the simulations. From the denoised channels $\tilde{h}$ and the simulated data $\hat{h}$, we can calculate the spectral efficiency C measured in units of bits per second per hertz on each subcarrier n as

$$C = \frac{1}{N} \sum_{n=1}^{N} \sum_{k=1}^{n_\lambda} \log_2 \left(1 + \frac{\sigma}{n_t \cdot \eta} \lambda_{n,k}^2 \right) \tag{14}$$

where $\lambda_{n,k}$ are the singular values of the matrix $\mathbf{H}_n$ and η is the average path gain

$$\eta = \frac{1}{n_r n_t N} \sum_{r=1}^{n_r} \sum_{t=1}^{n_t} \sum_{n=1}^{N} |\mathbf{H}_{r,t,n}|^2. \tag{15}$$

If we further assume a fixed SNR σ of 10 dB, then the results depend only on the structure of the channel matrix and the received power has no influence. This is especially useful when we want to study the effect of different antenna configurations on the spatial properties of the single-link MIMO channel. The results then focus on three key aspects: the structure of the channel matrix (i.e., the average power of each MIMO link), the distribution of the singular values, and the channel capacity.

IV. Model Validation by Measurement Results

A. A Simple Laboratory Test

At first, we verify the model by a simple measurement at 5 GHz in a LOS scenario in the laboratory [27] where the polarization rotation is evident. The transmitter and the receiver were fixed on tripods at the same height. Both were raised highly (≈2.5 m) in the air to reduce multipath effects. Two cross-polarized patch antennas were aligned on the optical axis facing each other. The transmitter was rotated from $-90°$ to 90° around the axis. The real and imaginary parts of the channel coefficients were then measured for each angle using a vector network analyzer. Each real and imaginary part was normalized by its maximum.

The scenario was reproduced in the model where the rotation of the antenna was done as described in Appendix A. The measured and simulated channel coefficients are plotted in Fig. 7. By following the traces in the figure, it is easily verified that the channel coefficients can be expressed by

$$\mathbf{H} = \begin{pmatrix} h_{\mathrm{vv}} & h_{\mathrm{vh}} \\ h_{\mathrm{hv}} & h_{\mathrm{hh}} \end{pmatrix} = \sqrt{2} e^{\frac{-i\pi}{4}} \begin{pmatrix} \cos\vartheta_p & \sin\vartheta_p \\ -\sin\vartheta_p & \cos\vartheta_p \end{pmatrix} \tag{16}$$

where $\cos\vartheta_p$ is the variation of the copolarized components, while $\mp\sin\vartheta_p$ is found for V–H and H–V components. The minor phase variation in the measurement can be attributed to unequal lengths of the feeder cables. Note that Quitin *et al.* [26]

[3]The normalized delay follows from $m_l = \tau_l \cdot B$ where τ_l is the delay of the path in seconds and B is the bandwidth of 20 MHz.

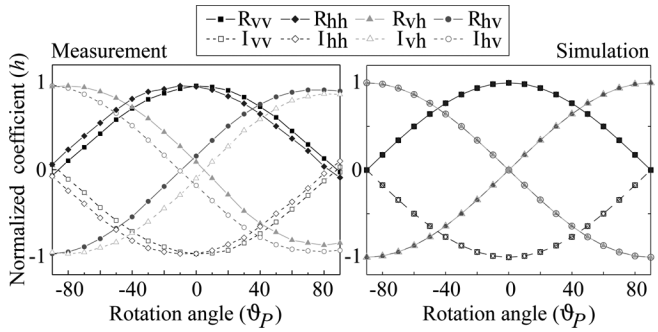

Fig. 7. Results of the laboratory test: The left plot shows the normalized channel coefficients from the measurement [27] and the right plot shows the results from the simulation. Both are identical except for a minor phase variation in the measurement due to imperfections in the setup.

could correctly predict similar observations with an analytical model.

B. Results of the Outdoor Measurements

An overview of the outdoor measurement results is given in Fig. 8. The figure shows five plots for each of the four scenarios. The top figures visualize the per-link power of the normalized MIMO matrix $\mathbf{H}/\eta$ where individual values were averaged over frequency and time. The left-hand side shows the results from the measurements, and the right-hand side shows the results from the simulations. The simulation results were additionally averaged over 30 independent iterations. The first four rows of each matrix plot represent the vertically polarized patches at the sides of the cube. Rows 5–8 are for the horizontally polarized sides and rows 9–10 are for the top patch. At the transmitter, the first eight links (Tx antenna index 1–8) are vertically polarized, and the second eight (index 9–16) are horizontally polarized. For all scenarios, both measurements and model are in good accordance with each other. The simulations are able to predict well the structure of the per-link power in the channel matrix. Small variations can be attributed to the antenna model in the simulations, the NLOS components, or the measurement noise. In the scenario TUB-Rx2, for example, there was a strong echo from the building north of the receiver. This reflection causes the strong power in rows 3 (vertical) and 6 (horizontal), which is not present in the simulation data.

The next two plots show the distribution of the singular values. The SVD orthogonalizes the MIMO channel matrix into subchannels. The magnitudes of the singular values thus characterize the spatial structure of the channel. Since we normalized the channel matrix by (15), those magnitudes scale with $\sum_{k=1}^{n_\lambda} \lambda_k^2 = n_t n_r$. Thus, if there is only one dominant singular value, it would have a size of $\sqrt{n_t n_r} \approx 12.6$. Two equally strong values would have magnitudes of $\sqrt{(n_t n_r)/2} \approx 8.9$. When there are only two dominant values λ_1 and λ_2, then at most two data streams can be transmitted in parallel although there are 16 transmit and ten receive antennas available. This is the case in all measured scenarios. There are always two dominant singular values with magnitudes between 6 and 10. The same is predicted by the simulations. Without NLOS components, the model predicts exactly two nonzero singular values due to the two independent polarizations. Smaller singular values come from NLOS paths. The differences of the distributions of the singular values are due to the different positions of the scatterers in the measurements and the simulations. It also seems that in the measurements, the smallest singular values are lager than in the simulations. This could be explained by noise and rounding offsets in the 8-b analog-to-digital (A/D) converters of the channel sounder.

The last plot shows the MIMO capacity distribution at a fixed SNR of 10 dB. The SNR limitation allows us to study the influence of the spatial channel structure without the received power. Similar evaluations were done in many references such as [12]. The gray shaded area shows the possible capacity range, the solid line shows the distribution of the measured capacities, and the dashed line shows the simulation results. Due to the 30 iterations, there is a slight variation in the simulation results. The range of these variations is illustrated by the errorbars showing the standard deviation ($\approx$1.4 b/s/Hz) of the percentiles of the empirical distribution function. A degenerated 10×16 channel with only one singular value, the so-called Keyhole channel [34], [35], has a capacity of 6.6 b/s/Hz (lower bound). Two equal singular values would result in 11.3 b/s/Hz. A channel matrix with independent and identically distributed (i.i.d.) coefficients would meet a capacity of 30 b/s/Hz and ten parallel channels would have 34.6 b/s/Hz (upper bound). Without NLOS components, the simulations predict an average capacity of 11.1 b/s/Hz in the four scenarios. This result is very close to the theoretical value for two independent streams. But note that the simulated capacity without NLOS components can never exceed 11.3 b/s/Hz for the reasons discussed above. The median measured capacities range from 14.2 to 19.2 b/s/Hz. Those values are slightly larger than the simulations results. However, in all cases, the simulations predict the capacity within 90% accuracy.

V. Conclusion and Discussion

The new model predicts the coefficients for the polarized LOS channel very well in all test cases. We confirm this by directly comparing the simulation results with measurements. To the authors' knowledge, this was not possible in earlier statistical channel models. The new approach can thus help to more accurately calculate the capacity in scenarios with a dominant LOS component. This is an important feature with many applications.

In cooperative cellular systems, for example, multiple-antenna terminals simultaneously communicate with several multiple-antenna BSs [36], [37]. In this case, the channel matrix at the receiver is a composition of the individual channels to all BSs, and the probability of one or more free LOS links is increased compared to single-link systems. The LOS power is dominant in the overall channel, and the use of cross-polarized antennas has a strong influence on the applicability of the interference mitigation strategies. The evaluation of such systems (e.g., [38] and [39]) is often based on the SCM or WINNER models and accurate polarization modeling is a crucial feature to predict the performance. Another example lies in satellite communications where MIMO becomes an increasingly interesting technique to enhance the achievable throughput [40]. However, the long distance between the transmitter and the receiver reduces the link to an effective Keyhole channel with only one

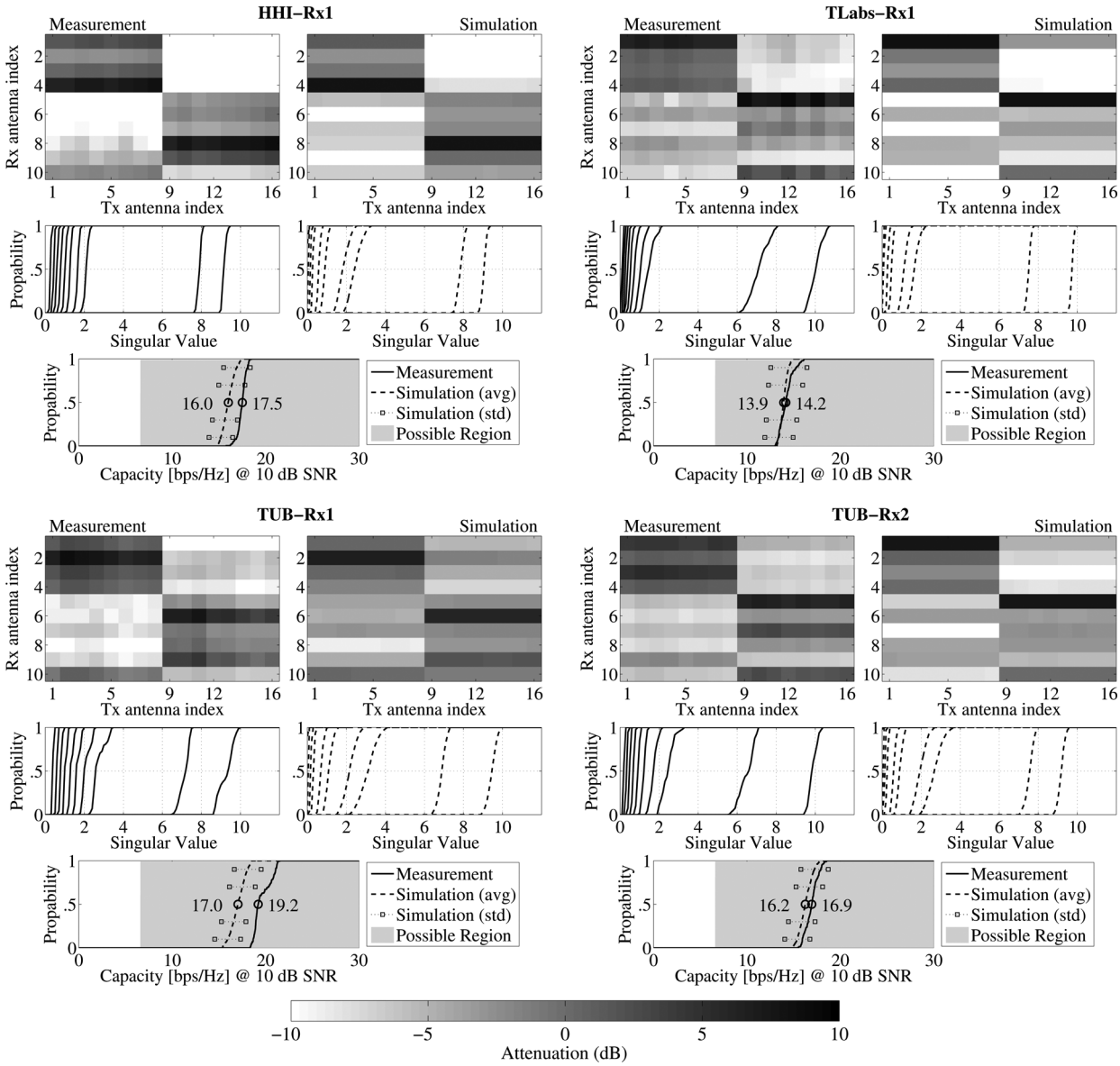

Fig. 8. Measurement results. See Section IV for details.

transmission path. MIMO gains can thus only result from polarization diversity. Again, the use of the proposed model can help to create accurate channel coefficients for such systems.

Nevertheless, the proposed method is just a model of the reality. A closer examination of the results in Fig. 8 shows minor discrepancies between simulation and reality. It is not clear if all of them can be explained by the existence of additional multipath effects in the measurements or anomalies in the antenna patterns. Another implication of the analogy between the antenna model [21], [25] and the Jones calculus [18] is that technically the WINNER model always creates polarized signals. It is therefore not possible to support unpolarized electromagnetic waves.

As we have discussed in Section II-E, it is likely that the polarization coupling matrix for the NLOS components has complex entries and scattered waves are elliptically polarized. This is also indicated in [29] and [30]. We model this effect by introducing a phase shift κ between the vertical and horizontal components of the scattered waves in (11). However, the distribution of κ is an open issue. One possible improvement of the model can thus be made by including measured statistics of κ.

Appendix A
Changing the Orientation of Antennas

An antenna pattern (2) is given in spherical coordinates as a function of the azimuth angle ϕ and the elevation angle θ. When the orientation of the antenna element changes, the field pattern has to be read at different angles (Φ, Θ) which include the effect of the orientation change. Rotations in 3-D are easier in Cartesian coordinates. Therefore, we transform the original angle pair

(ϕ, θ) into a vector $\mathbf{a}$ that describes the arrival or departure angles in Cartesian coordinates. The three vector elements represent the x-, y-, and z-components

$$\mathbf{a}(\phi,\theta) = \begin{pmatrix} \cos\phi \cdot \cos\theta \\ \sin\phi \cdot \cos\theta \\ \sin\theta \end{pmatrix}. \tag{17}$$

We now use a 3×3 matrix $\mathbf{Q}$ to describe the orientation change in 3-D space. In principal, we can calculate $\mathbf{Q}^T$ for any arbitrary rotation axis and angle. The example in Fig. 2 was tilted by 20° around the x-axis of the coordinate system. The corresponding matrix is

$$\mathbf{Q}_x(20^\circ) = \begin{pmatrix} 1 & 0 & 0 \\ 0 & \cos(20^\circ) & -\sin(20^\circ) \\ 0 & \sin(20^\circ) & \cos(20^\circ) \end{pmatrix}. \tag{18}$$

By multiplying $\mathbf{Q}$ with (17), we include the orientation change in the vector

$$\mathbf{a}^+(\phi,\theta) = \mathbf{Q}^T \cdot \mathbf{a}(\phi,\theta). \tag{19}$$

Since $\mathbf{a}^+$ is now also in Cartesian coordinates and we need the transformed pattern $\tilde{\mathbf{F}}$ in spherical coordinates, we have to transform $\mathbf{a}^+$ back to spherical coordinates. This results in the new angles (Φ, Θ)

$$\Phi(\phi,\theta) = \arctan_2\left[a_y^+(\phi,\theta), a_x^+(\phi,\theta)\right] \tag{20}$$

$$\Theta(\phi,\theta) = \arcsin\left[a_z^+(\phi,\theta)\right]. \tag{21}$$

a_x^+, a_y^+, and a_z^+ are the x-, y-, and z-components of $\mathbf{a}^+$, respectively. We now get the coefficients of the rotated pattern by reading the original pattern $\mathbf{F}$ at the transformed angles

$$\hat{F}_{\frac{\mathrm{V}}{\mathrm{H}}}(\phi,\theta) = F_{\frac{\mathrm{V}}{\mathrm{H}}}(\Phi,\Theta). \tag{22}$$

Since the patterns are sampled at a fixed angular grid, this involves an interpolation step. As a standard computationally inexpensive procedure, we use linear interpolation. Alternatively, more advanced techniques based on the effective aperture distribution function (EADF) can be used [25].

The second step of the transformation takes the polarization into account. First, we take the antenna orientation vector $\mathbf{o}$ and apply the rotation matrix $\mathbf{Q}$ to obtain $\tilde{\mathbf{o}}$

$$\tilde{\mathbf{o}} = \mathbf{Q} \cdot \mathbf{o}. \tag{23}$$

This vector $\tilde{\mathbf{o}}$ is the new orientation vector of the transformed pattern. Next, we calculate a rotation matrix that accounts for the changed polarization characteristics of the rotated antenna pattern. In principal, the following procedure emulates an antenna measurement like in an anechoic chamber. The virtual transmitter is placed south of our test antenna. The wave travel direction $\mathbf{r}$ thus lies in the y-direction. We rotate the orientation vector of our antenna so that it matches the wave travel direction. The polarization vector $\mathbf{p}_r$ results from a projection of the orientation vector $\mathbf{o}_r$ on the plane perpendicular to the travel direction (see Fig. 4 for details).

1) We rotate the orientation vector $\tilde{\mathbf{o}}$ by $p = -\phi - \pi/2$ in the azimuth direction and $q = \theta$ in the elevation direction to match the orientation of the transmitter

$$\mathbf{o}^+ = \begin{pmatrix} \cos p & -\sin p & 0 \\ \cos q \cdot \sin p & \cos q \cdot \cos p & -\sin q \\ \sin q \cdot \sin p & \sin q \cdot \cos p & \cos q \end{pmatrix} \cdot \tilde{\mathbf{o}}. \tag{24}$$

2) We calculate the projection of the orientation vector on the projection plane. Since the projection plane lies in the $x - z$-plane due to the placement of the transmitter, we simply omit the y-component of $\mathbf{o}^+$, switch the x- and z-components, and normalize the resulting vector to unit length. The switching is done to obtain the same orientation as in (2)

$$\mathbf{p}_r = \frac{\begin{pmatrix} o_z^+ \\ o_x^+ \end{pmatrix}}{\left|\begin{pmatrix} o_z^+ \\ o_x^+ \end{pmatrix}\right|}. \tag{25}$$

3) We define the transmitter to be either perfectly vertical ($\mathbf{p}_t = [1,0]^T$) or perfectly horizontal ($\mathbf{p}_t = [0,1]^T$). As a consequence, the product $\mathbf{p}_r^T \cdot \mathbf{p}_t$ selects either the vertical component or the horizontal component of $\mathbf{p}_r$, and α can be calculated as

$$\alpha = \arctan_2(p_{ry}, p_{rx}) = \arctan_2\left(o_x^+, o_z^+\right). \tag{26}$$

4) α is the angle between the projection of the orientation vector and the E_x component of the transmit polarization. Since the transmitter is vertically polarized, β_t is 0. The angle β_r comes from the rotated field pattern response (22)

$$\beta_r = \arctan_2\left\{\hat{F}_H(\phi,\theta), \hat{F}_V(\phi,\theta)\right\}. \tag{27}$$

5) The difference between α and β_r is the rotation angle ϑ, which is used to calculate the polarization effects on the pattern. The rotated pattern then notes

$$\vartheta = -\beta_r - \alpha$$

$$\tilde{\mathbf{F}}(\phi,\theta) = \begin{pmatrix} \cos\vartheta & -\sin\vartheta \\ \sin\vartheta & \cos\vartheta \end{pmatrix} \cdot \begin{pmatrix} \hat{F}_{\mathrm{V}}(\phi,\theta) \\ \hat{F}_{\mathrm{H}}(\phi,\theta) \end{pmatrix}. \tag{28}$$

Appendix B
Calculating the Offset Angle ϑ for LOS Links

Here, we describe how the offset angle ϑ for the polarization rotation matrix (5) is calculated for the LOS component.

1) To simplify the computations, we rotate the coordinate system (and thus the receiver orientation vector $\mathbf{o}_r$) by $p = -\phi^a - \pi/2$ in the azimuth direction and $q = \theta^a$ in the elevation direction such that the wave travel direction $\mathbf{r}$ lies in the y-direction (i.e., $\mathbf{r}^+ = (0,1,0)^T$).[4]
2) We calculate the projection of the receiver orientation vector $\mathbf{o}_r$ on the projection plan.[5]

[4]This is the same as step 1 in Appendix A; see (24).

[5]This is the same as step 2 in Appendix A; see (25).

3) We get the transmit polarization vector $\mathbf{p}_t$ by normalizing the field pattern vector $\mathbf{F}_t$ (2) to unit length.[6] $\mathbf{F}_t$ is already in the same plane as $\mathbf{p}_r$ due to the coordinate rotation

$$\mathbf{p}_t = \frac{\mathbf{F}_t}{|\mathbf{F}_t|}. \tag{29}$$

4) We calculate the angle α between the two vectors

$$\alpha = \arccos\left(\mathbf{p}_r^T \cdot \mathbf{p}_t\right). \tag{30}$$

5) We obtain the angles β_t and β_r from the field patterns of the transmitter and the receiver, respectively. $\beta_{t/r}$ is the angle between the x-axis of the polarization plane and the polarization vector

$$\beta_t = \arctan_2\left\{F_{tH}(\phi^d, \theta^d), F_{tV}(\phi^d, \theta^d)\right\} \tag{31}$$
$$\beta_r = \arctan_2\left\{F_{rH}(\phi^a, \theta^a), F_{rV}(\phi^a, \theta^a)\right\}. \tag{32}$$

6) The difference between the angles β_t and β_r is the polarization mismatch β between the receiver and the transmitter if both antenna elements were aligned on the same optical axis. The angle α, however, takes the different orientation of the receive antenna into account. We thus need to rotate the polarization of the receiver by an angle of

$$\vartheta_{r,t} = \beta_t - \beta_r - \alpha. \tag{33}$$

Appendix C
Modeling Circular-Polarized Antennas

As mentioned in Section II, the dual-polarized field pattern can be interpreted as a Jones vector which describes the polarization state of the ray. In many applications, such as satellite communications, circular polarization is needed. A straightforward extension would use complex coefficients in the field patterns where

$$\mathbf{F}_{\mathrm{R}} = \frac{1}{\sqrt{2}}\begin{pmatrix}1\\ i\end{pmatrix} \quad \mathbf{F}_{\mathrm{L}} = \frac{1}{\sqrt{2}}\begin{pmatrix}1\\ -i\end{pmatrix} \tag{34}$$

are the Jones vectors for the right-hand circular-polarized (RHCP) and left-hand circular-polarized (LHCP) signals, respectively. However, in order to use the LOS model from Section II-D, we need an antenna orientation vector $\mathbf{o}$ which is aligned with a vertically polarized antenna. This is not possible here and, thus, predicting the LOS polarization will lead to erroneous results in some cases. A solutions is to virtually assemble a circular-polarized antenna out of two linear elements. These elements need to be crossed in a way that the transmission axes of both elements are perpendicular to each other. Both elements are fed with the same signal, but one of them is shifted by 90° out of phase. This is modeled by using the channel coefficients (1) for each of the two elements and assembling them in a channel matrix $\mathbf{G}$. In order to get circular-polarized coefficient matrix $\mathbf{G}^\circ$, we use the Jones vectors (34) as coupling matrices

$$\mathbf{G}^\circ = \begin{pmatrix} g_{\mathrm{RR}} & g_{\mathrm{RL}} \\ g_{\mathrm{LR}} & g_{\mathrm{LL}} \end{pmatrix} = \mathbf{C}^H \mathbf{G} \mathbf{C} = \frac{1}{2}\begin{pmatrix}1 & -i\\ 1 & i\end{pmatrix}\begin{pmatrix} g_{\mathrm{VV}} & g_{\mathrm{VH}} \\ g_{\mathrm{HV}} & g_{\mathrm{HH}} \end{pmatrix}\begin{pmatrix}1 & 1\\ i & -i\end{pmatrix}. \tag{35}$$

In order to verify this calculation, we repeat the simulations from Section IV-A with the coupling matrices from above. The results are depicted in Fig. 9. The transmitter is rotated around the optical axis. Real and imaginary parts of the signal are out of phase by 90°, and cross talk between the elements is suppressed, which is typical for this setup.

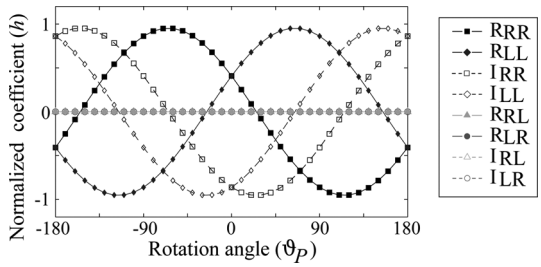

Fig. 9. Results of the simulation with circular-polarized antennas.

Appendix D
Model of the Measurement Antenna

Both transmit and receive antennas are built from single patch elements. The antenna pattern of the entire arrays was measured in an anechoic chamber. A single element of the receiver cube has an FWHM of 90° and a front-to-back ratio of 10 dB. We first created a model of the element by matching its azimuth and elevation response to the measurement. The vertically polarized antenna response was then modeled as

$$\begin{aligned} F(\phi,0) &= 0.1 + 0.9 \cdot \exp(-1.315 \cdot \phi^2) \\ F(0,\theta) &= \cos(\theta)^2 \\ F(\phi,\theta) &= \begin{cases} F(\phi,0)F(0,\theta), & F(\phi,0)F(0,\theta) > 0.1 \\ 0.1, & \text{otherwise} \end{cases} \end{aligned} \tag{36}$$

where $\phi = -\pi \ldots \pi$ and $\theta = -(\pi/2) \ldots (\pi/2)$ are the azimuth and elevation angles, respectively. We placed the elements at the sides of the cube by applying the technique from Appendix A. The transmitter has a reduced FWHM in the elevation direction of 20° and sidelobes with a maximum power of -15 dBi. We thus approximated the pattern to

$$\begin{aligned} F(\phi,0) &= 0.03 + 0.97 \cdot \exp(-1.175 \cdot \phi^2) \\ F(0,\theta) &= \cos(\theta)^{45.3} \\ F(\phi,\theta) &= \begin{cases} F(\phi,0)F(0,\theta), & F(\phi,0)F(0,\theta) > 0.03 \\ 0.03, & \text{otherwise.} \end{cases} \end{aligned} \tag{37}$$

This pattern was then used for the vertical component of the first eight elements and the horizontal component of the elements 9–16. The orientation vector was turned accordingly. The entire array was then rotated to match the sector orientations.

[6]Since the transmit antenna is rotated by the method from Appendix A, $\mathbf{F}_t$ and the projection of $\mathbf{o}_t$ on the plane yield identical results for $\mathbf{p}_t$.

ACKNOWLEDGMENT

The authors would like to thank A. Brylka and U. Krüger [Heinrich Hertz Institute (HHI), Berlin, Germany] for constructing the antenna arrays; G. Sommerkorn and M. Landmann [Ilmenau University of Technology (IUT), Ilmenau, Germany] for the calibration of the arrays; S. Warzügel (MEDAV GmbH, Uttenreuth, Germany) for operating the channel sounder; Y. Hadisusanto, L. Jiang, T. Wirth, M. Mehlhose, S. Schiffermüller, A. Brylka (HHI), G. Sommerkorn, and A. Hong (IUT) for their assistance during the measurements, L. Jiang for help with the laboratory measurements, V. Venkatkumar and L. Raschkowski (HHI) as well as E. Eberlein and F. Burkhardt (Fraunhofer IIS, Erlangen, Germany) for the fruitful discussions; and Prof. Dr. R. Thomä, M. Käske, and C. Schneider (IUT) for their valuable comments on the manuscript.

REFERENCES

[1] G. Foschini and M. Gans, "On limits of wireless communications in a fading environment when using multiple antennas," *Wireless Pers. Commun.*, no. 3, pp. 311–335, 1998.

[2] M. Jensen and J. Wallace, "A review of antennas and propagation for MIMO wireless communications," *IEEE Trans. Antennas Propag.*, vol. 52, no. 11, pp. 2810–2824, Nov. 2004.

[3] *Air Interface for Broadband Wireless Access Systems*, IEEE Std 802.16-2009 Part 16, 2009.

[4] "Technical specification group radio access network; evolved universal terrestrial radio access (E-UTRA)," Tech. Rep. 3GPP TR 36.814 v9.0.0 (release 9), 2010.

[5] "Spatial channel model for multiple input multiple output (MIMO) simulations," Tech. Rep. 3GPP TR 25.996 v10.0.0, 2011.

[6] P. Kyösti, J. Meinilä, and L. Hentilä, "IST-4-027756 WINNER II D1.1.2 v.1.1: WINNER II channel models," Tech. Rep., 2007.

[7] P. Heino, J. Meinilä, P. Kyösti, L. Hentilä, T. Jämsä, E. Suikkanen, E. Kunnari, and M. Narandzic, "CELTIC/CP5-026 D5.3: WINNER+Final channel models," Tech. Rep., 2010.

[8] C. Schneider, M. Narandzic, M. Käske, G. Sommerkorn, and R. Thomä, "Large scale parameter for the WINNER II channel model at 2.53 GHz in urban macro cell," in *Proc. IEEE Veh. Technol. Conf.*, 2010, DOI: 10.1109/VETECS.2010.5494089.

[9] M. Narandzic, C. Schneider, M. Käske, S. Jaeckel, G. Sommerkorn, and R. Thomä, "Large-scale parameters of wideband MIMO channel in urban multi-cell scenario," in *Proc. Eur. Conf. Antennas Propag.*, 2011, pp. 3759–3763.

[10] ITU-R, "Guidelines for evaluation of radio interface technologies for IMT-Advanced," Tech. Rep. ITU-R M.2135-1, 2009.

[11] K. Bakowski and K. Wesolowski, "Change the channel," *IEEE Veh. Technol. Mag.*, vol. 6, no. 2, pp. 82–91, Jun. 2011.

[12] D. Chizhik, J. Ling, P. Wolniansky, R. Valenzuela, N. Costa, and K. Huber, "Multiple-input-multiple-output measurements and modeling in Manhattan," *IEEE J. Sel. Areas Commun.*, vol. 21, no. 3, pp. 321–331, Apr. 2003.

[13] V. Jungnickel, S. Jaeckel, L. Thiele, L. Jiang, U. Krüger, A. Brylka, and C. Helmolt, "Capacity measurements in a cooperative multicell MIMO network," *IEEE Trans. Veh. Technol.*, vol. 58, no. 5, pp. 2392–2405, Jun. 2009.

[14] S. Jaeckel, L. Thiele, and V. Jungnickel, "Interference limited MIMO measurements," in *Proc. IEEE Veh. Technol. Conf.*, 2010, DOI: 10.1109/VETECS.2010.5494108.

[15] M. R. Andrews, P. P. Mitra, and R. de Carvalho, "Tripling the capacity of wireless communications using electromagnetic polarization," *Nature*, vol. 409, pp. 316–318, Jan. 2001.

[16] A. Weber and A. Bestard, "Modeling of X-Pol antennas for LTE system simulation," in *Proc. IEEE Int. Symp. Wireless Commun. Syst.*, 2011, pp. 221–225.

[17] Y. Zhou, S. Rondineau, D. Popovic, A. Sayeed, and Z. Popovic, "Virtual channel space-time processing with dual-polarization discrete lens antenna arrays," *IEEE Trans. Antennas Propag.*, vol. 53, no. 8, pp. 2444–2455, Aug. 2005.

[18] R. C. Jones, "A new calculus for the treatment of optical systems—I. Description and discussion of the calculus," *J. Opt. Soc. Amer.*, vol. 31, pp. 488–493, Jul. 1941.

[19] L. Thiele, M. Peter, and V. Jungnickel, "Statistics of the Ricean K-factor at 5.2 GHz in an urban macro-cell scenario," in *Proc. IEEE Int. Symp. Pers. Indoor Mobile Radio Commun.*, 2006, DOI: 10.1109/PIMRC.2006.254301.

[20] C. Oestges, V. Erceg, and A. Paulraj, "Propagation modeling of MIMO multipolarized fixed wireless channels," *IEEE Trans. Veh. Technol.*, vol. 53, no. 3, pp. 644–654, May 2004.

[21] M. Shafi, M. Zhang, A. Moustakas, P. Smith, A. Molisch, F. Tufvesson, and S. Simon, "Polarized MIMO channels in 3-D: Models, measurements and mutual information," *IEEE J. Sel. Areas Commun.*, vol. 24, no. 3, pp. 514–527, Mar. 2006.

[22] V. Erceg, H. Sampath, and S. Catreux-Erceg, "Dual-polarization versus single-polarization MIMO channel measurement results and modeling," *IEEE Trans. Wireless Commun.*, vol. 5, no. 1, pp. 28–33, Jan. 2006.

[23] M. Landmann, K. Sivasondhivat, J. Takada, and R. Thomä, "Polarisation behaviour of discrete multipath and diffuse scattering in urban environments at 4.5 GHz," *EURASIP J. Wireless Commun. Netw.*, vol. 2007, no. 1, pp. 60–71, 2007.

[24] C. Oestges, B. Clerckx, M. Guillaud, and M. Debbah, "Dual-polarized wireless communications: From propagation models to system performance evaluation," *IEEE Trans. Wireless Commun.*, vol. 7, no. 10, pp. 4019–4031, Oct. 2008.

[25] M. Narandzic, M. Käske, C. Schneider, M. Milojevic, M. Landmann, G. Sommerkorn, and R. Thomä, "3D-antenna array model for IST-WINNER channel simulations," in *Proc. IEEE Veh. Technol. Conf.*, 2007, pp. 319–323.

[26] F. Quitin, C. Oestges, F. Horlin, and P. De Doncker, "Multipolarized MIMO channel characteristics: Analytical study and experimental results," *IEEE Trans. Antennas Propag.*, vol. 57, no. 9, pp. 2739–2745, Sep. 2009.

[27] L. Jiang, L. Thiele, and V. Jungnickel, "On the modelling of polarized MIMO channel," in *Proc. Eur. Wireless Conf.*, 2007.

[28] T. Svantesson, "A physical MIMO radio channel model for multi-element multi-polarized antenna systems," in *Proc. IEEE Veh. Technol. Conf.*, 2001, vol. 2, pp. 1083–1087.

[29] L. Materum, J. Takada, I. Ida, and Y. Oishi, "Mobile station spatio-temporal multipath clustering of an estimated wideband MIMO double-directional channel of a small urban 4.5 GHz macrocell," *EURASIP J. Wireless Commun. Netw.*, 2009, article # 9.

[30] F. Quitin, C. Oestges, F. Horlin, and P. De Doncker, "A polarized clustered channel model for indoor multiantenna systems at 3.6 GHz," *IEEE Trans. Veh. Technol.*, vol. 59, no. 8, pp. 3685–3693, Aug. 2010.

[31] J. Poutanen, K. Haneda, L. Liu, C. Oestges, F. Tufvesson, and P. Vainikainen, "Parameterization of the COST 2100 MIMO channel model in indoor scenarios," in *Proc. Eur. Conf. Antennas Propag.*, 2011, pp. 3606–3610.

[32] R. Thomä, D. Hampicke, A. Richter, G. Sommerkorn, and U. Trautwein, "MIMO vector channel sounder measurement for smart antenna system evaluation," *Eur. Trans. Telecommun.*, vol. 12, pp. 427–438, 2001.

[33] G. W. Stewart, "On the early history of the singular value decomposition," Institute for Adv. Comput. Studies, Univ. Maryland, College Park, MD, Tech. Rep. TR-92-31, 1992.

[34] D. Chizhik, G. Foschini, and M. Gans, "Keyholes, correlations and capacities of multielement transmit and receive antennas," *IEEE Trans. Wireless Commun.*, vol. 1, no. 2, pp. 361–368, Apr. 2002.

[35] S. Loyka and A. Kouki, "On MIMO channel capacity, correlations, and keyholes: Analysis of degenerate channels," *IEEE Trans. Commun.*, vol. 50, no. 12, pp. 1886–1888, Dec. 2002.

[36] H. Zhang and H. Dai, "Cochannel interference mitigation and cooperative processing in downlink multicell multiuser MIMO networks," *EURASIP J. Wireless Commun. Netw.*, vol. 2004, no. 2, pp. 222–235, 2004.

[37] M. Karakayali, G. Foschini, and R. Valenzuela, "Network coordination for spectrally efficient communications in cellular systems," *IEEE Wireless Commun. Mag.*, vol. 13, no. 4, pp. 56–61, Aug. 2006.

[38] A. Tölli, M. Codreanu, and M. Juntti, "Cooperative MIMO-OFDM cellular system with soft handover between distributed base station antennas," *IEEE Trans. Wireless Commun.*, vol. 7, no. 4, pp. 1428–1440, Apr. 2008.

[39] V. Jungnickel, M. Schellmann, L. Thiele, T. Wirth, T. Haustein, O. Koch, E. Zirwas, and E. Schulz, "Interference aware scheduling in the multiuser MIMO-OFDM downlink," *IEEE Commun. Mag.*, vol. 47, no. 6, pp. 56–66, Jun. 2009.

[40] P. Arapoglou, E. Michailidis, A. Panagopoulos, A. Kanatas, and R. Prieto-Cerdeira, "The land mobile Earth-space channel," *IEEE Veh. Technol. Mag.*, vol. 6, no. 2, pp. 44–53, Jun. 2011.

Stephan Jaeckel (S'10–M'12) was born in Freiberg, Germany, in 1982. He received the B.Eng. and M.Eng. degrees in information and communications technology from Hochschule für Telekommunikation, Leipzig, Germany, in 2005 and 2007, respectively. He is currently working toward the Dr. Ing. (Ph.D.) degree in electrical engineering at the Ilmenau University of Technology (IUT), Ilmenau, Germany.

In 2006, he was a summer student at CERN, Geneva, Switzerland, where he worked on the software for the LHCb particle detector. In 2007, he joined the Fraunhofer Heinrich Hertz Institute, Berlin, Germany, where he worked on the measurement-based performance analysis of cooperative mobile communication systems. His current research interests include measurements and data analysis in heterogenous multicell networks including relays as well as channel modeling for terrestrial and satellite systems.

Kai Börner (S'12) received the Dipl.-Ing. (M.S.) degree in electrical engineering from the Technische Universität Berlin, Berlin, Germany, in 2009, where he is currently working toward the Dr.-Ing. (Ph.D.) degree in electrical engineering.

He joined the Fraunhofer Heinrich Hertz Institute (HHI), Berlin, Germany, in April 2009. His research interests lie in channel modeling, energy-efficient transmission and self-organization in heterogeneous multiple-input–multiple-output (MIMO) orthogonal frequency-division multiplexing (OFDM)-based networks.

Lars Thiele (S'06–M'09) received the Dipl.-Ing. (M.S.) degree in electrical engineering from the Technische Universität Berlin, Berlin, Germany, in 2005. Currently, he is working toward the Dr.-Ing. (Ph.D.) degree in electrical engineering at the Technical University of Munich (TUM), Munich, Germany and the Fraunhofer Heinrich Hertz Institute (HHI), Berlin, Germany.

He joined the Fraunhofer HHI in September 2005. He has contributed to receiver and transmitter optimization under limited feedback, performance analysis for multiple-input–multiple-output (MIMO) transmission in cellular orthogonal frequency-division multiplexing (OFDM) systems, fair-resource allocation, and cooperative multipoint (CoMP) transmission under constrained channel state information at the transmitter. He has authored and coauthored about 40 conference and journal papers as well as a couple of book chapters in the area of mobile communications. He leads the System Level Innovation research group at Fraunhofer HHI.

Volker Jungnickel (M'00) received the Dipl.-Phys. (M.Sc.) and Dr.rer.nat. (Ph.D.) degrees in experimental physics from Humboldt University of Berlin, Berlin, Germany, in 1992 and 1995, respectively.

He is a Lecturer at the Technical University, Berlin, Germany. He has worked on photoluminescence of semiconductor quantum dots and minimally invasive laser surgery before joining the Fraunhofer Heinrich Hertz Institute (HHI), Berlin, Germany, in 1997. After completing a 155-Mb/s wireless indoor communications link based on infrared light, he focused his research on broadband multiple-input–multiple-output (MIMO) systems. He has recently completed a 1-Gb/s MIMO–OFDM radio link in real time. His current research is concerned with next-generation cellular systems.